EFFECT OF CONTROLLED PERIODIC ROUGHNESS ON GOERTLER VORTICES IN HYPERSONIC COMPRESSION RAMP FLOW

P.V. Chuvakhov,[*,] V.N. Radchenko,[*] E.A. Alexandrova,[*,**] and V.Ya. Borovoy[*]**
[*]Central Aerohydrodinamic Institute (TsAGI)
[**]Moscow Institute of Physics and Technology (MIPT)

Keywords: *hypersonic, compression corner, heat transfer, Görtler vortices*

Abstract

Controlled experiments on heat transfer are carried out in shock wind tunnel UT-1M (TsAGI) for Mach 8 15° compression corner flow affected by Goertler-like vortices. Experiments cover two Reynolds numbers: $Re_{\infty L}=(1.75\pm0.09)\times10^5$ and $(3.90\pm0.09)\times10^5$ based on the sharp flat plate length. The effect of streamwise vortices of different intensity on the mean level of heat flux and its variation at the reattachment region is investigated. Intensity of vortices is varied by variation of the height of spanwise rake of cylindrical pins (seeding elements) placed on the plate ahead of the separation bubble.

1 Introduction

Design of heat protection systems for control surfaces of aerospace vehicles (elevons, flaps) gives rise to a fundamental problem of supersonic flow in a compression corner. Flow reattachment may lead to excessive heat flux regions and form favorable conditions for Görtler vortices to occur. Such vortices are seeded by surface irregularities that also determine the vortices intensity. Being amplified in the reattachment region, the vortices may result in considerable variations of heat flux with amplitudes up to 100% of its spanwise-averaged value (see, e.g., [1]). The presence of vortices may also increase the mean value of heat flux, which is commonly connected to transitional state of the reattachment flow [2]. However, numerical investigations [1, 3] showed that this may happen in a purely laminar flow. Though different in nature, similar effect was observed in direct numerical simulation [4] of fundamental breakdown on Mach 6 cone where regular streamwise streaks occurred because of nonlinear processes and caused sharp increase of heat flux before the transition to turbulence took over.

The purpose of the present study is to support numerical findings of [1, 3] experimentally, thereby revealing the effect of the intensity of Görtler-like vortices on the mean level and variations of heat flux in the reattachment region. To this effect, the vortices are seeded ahead of the separation bubble by a spanwise rake of cylindrical roughness elements of same height. Varying the height allows to change the intensity of the vortices

2 General information on the experiments

The test model is a flat plate of 320×150 mm shown in Fig. 1 with a 15° wedge installed on the top. The plate consists of the fiberglass insert 1 flash mounted into a steel frame. The wedge (ramp) is a strait triangular prism of steel with the insert 2 of Plexiglas. A part of the wedge under flow is 150 mm long. The sidewalls are designed both for the plate and for the wedge to preserve nominally two-dimensional base flow.

The hinge line (the corner line) is located at L=50 mm apart from an exchangeable sharp leading edge (see Fig. 2; the edge thickness is 21±1 μm). The streamwise length of the leading edge element is 27 mm. It connects tightly with the plate frame to form a single plane. The possible imperfection of the connection is uniform in spanwise direction and designed to be an upward-facing step with less than 10μm

height. The step is at the bottom of the boundary layer (BL) for the present experiments and does not affect the flow; the corresponding value of Re_{kk} is well under 25 [5].

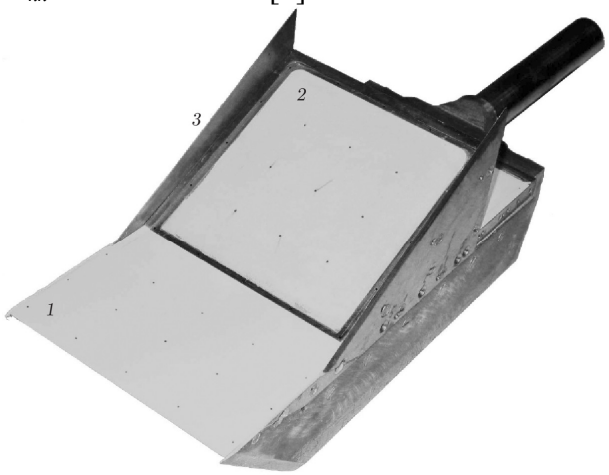

Fig. 1. Experimental model

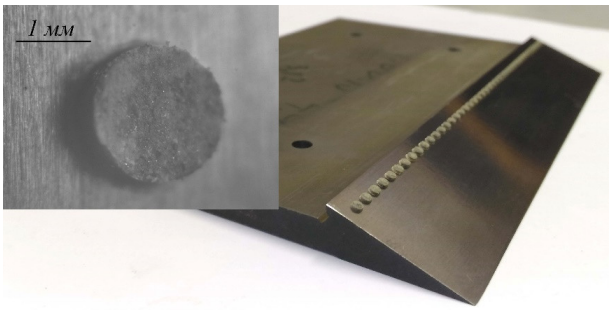

Fig. 2. Example of roughness on the leading edge element (x_k=23.5 mm for present picture only)

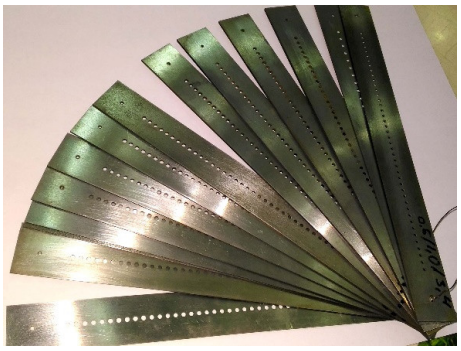

Fig. 3. Templates for roughness rake formation

Vortices intensity is varied in experiments by changing the intensity of steady disturbances ahead of the separation bubble. The disturbances develop behind a rake of cylindrical roughness elements distributed periodically in spanwise direction at x_k=17 mm apart from the leading edge, as shown in Fig. 2. The diameter of the elements is 1.7±0.1 mm, the spacing is 3.4±0.1 mm. The roughness is formed by using specially designed steel templates, Fig. 3 of thickness from 0.1 to 1.6 mm with two-component solidifying polyester composition that is put onto the metal surface of the leading edge through the templates. Six sharp (21±1 μm) leading edges are manufactured and polished, with the surface roughness measured within 0.8 μm.

Experiments are carried out in shock wind tunnel UT-1M (TsAGI) at Mach number 8, stagnation temperature T_0≈735±5 K and two values of total pressure p_0=15.5±0.7 and 34.1±1.3 bar. The corresponding unit Reynolds numbers are $Re_{\infty,1} = (3.55 \pm 0.16) \times 10^6$ and $(7.79\pm0.30) \times 10^6$ m^{-1}, which gives the value of $Re_{\infty,L}= (1.77 \pm 0.08) \times 10^5$ and $(3.90\pm 0.15) \times 10^5$ based on the hinge line station L=50 mm. The experiments are hereafter labeled in accord with the value of Reynolds number as group '#1' and '#3' for the lower and the higher values, respectively. The chosen parameters correspond to laminar (#1) or transitional (#3) state of the flow at reattachment region according to the criterion of [6]: $Re_{\infty,L} < 5\times10^5$. However, this criterion may depend on the wind tunnel in use.

The wind tunnel UT-1M operates in Ludwig scheme. The Mach 8 profiled nozzle with the exit diameter of 500 mm follows a lengthy heated high-pressure channel. A single run duration is about 40 ms with nearly constant flow characteristics in the test chamber.

Thermal effect of vortices is determined using panoramic patterns of heat flux over the flat plate and the wedge surfaces covered with thermal insulating material (over the inserts of fiberglass or Plexiglas). Such patterns are resulted from the thermal measurements of a surface temperature rise during a run by making use of temperature sensitive paints (TSP) developed in TsAGI. With known timing of a measurement, thermal properties the inserts (items 1 and 2 in Fig. 1), wall temperature and flow conditions, one can derive a heat flux from the flow to the surface and express it in the form of dimensionless heat flux coefficient hereafter referred to as Stanton number, St [7]:

$$\mathrm{St} = \frac{q_w}{\rho_\infty u_\infty c_p \left(T_0 - T_w\right)} = \frac{\mu_w/\mu_\infty}{\mathrm{Pr}\cdot \mathrm{Re}_{\infty,1}} \frac{1}{T_0 - T_w} \times \frac{dT}{d\vec{n}} \quad (1)$$

Repeatability of experiments was checked by doing several experiments again on different days or with a roughness rake remade.

3 Results

3.1 Schlieren visualization

Figures 4 and 5 illustrate the flow patterns in the presence of roughness rakes of different height. In case of no roughness, flow structure is usual for hypersonic compression corner flow (Fig. 4a, 5a). There is a bow shock wave generated by viscous interaction near the plate leading edge. A light curve near the surface marks the boundary layer development, starting at the leading edge and following downstream. The curve deviates from the surface ahead of the hinge line, which points to the station of the BL separation. Passing over the separation bubble, the curve comes back to the wedge surface at the station of BL reattachment. Maximum heat flux is observed near the thinnest part between the curve and the wedge surface that is commonly called as 'neck'. It is not straightforward how to measure the neck station; its approximate value is $x_{neck}\approx30$ mm for the cases k=0.0 mm and 0.6 mm (Fig. 4a and b). Separation and reattachment of flow produce the corresponding shock waves that propagate downstream, combine and interact with the bow shock wave forming the complicated flow pattern. There remains a hardly visible rest of the bow shock wave (Fig. 4a, 5c) downstream of the waves interaction that falls onto the surface measured from the hinge line, in particular, near the station x=71 mm in Fig. 4a. This station will be reminded during the analysis of TSP results.

One may note two features relative for laminar separated flow: 1) separation bubble is rather lengthy and its outer edge is inclined at small angle with respect to the plate surface; 2) the boundary layer curve is distinct behind the reattachment. This is better visible for the case without roughness and may point to the fact that the observed flow is not turbulent downstream the reattachment.

Adding the roughness rake has different effect at different Reynolds numbers seemingly because of different roughness height-to-BL thickness ratios at roughness station. For Re group #1, adding the roughness of height k<0.6 mm does not affect the separated flow much and only adds a shock wave from the roughness elements. The further increase of the height leads to slight increase of separation bubble size (see Fig. 4b for k=0.6 mm). This might be caused by entropy layer effect that appears due to the roughness protruding into the supersonic part of the boundary layer.

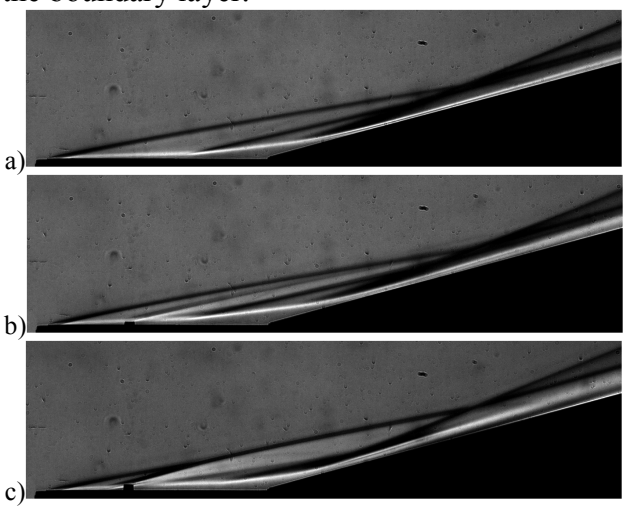

Fig. 4. Schlieren visualization, Re group #1. Roughness heights: 0.0 (a), 0.6 (b) and 1.2 (c) mm

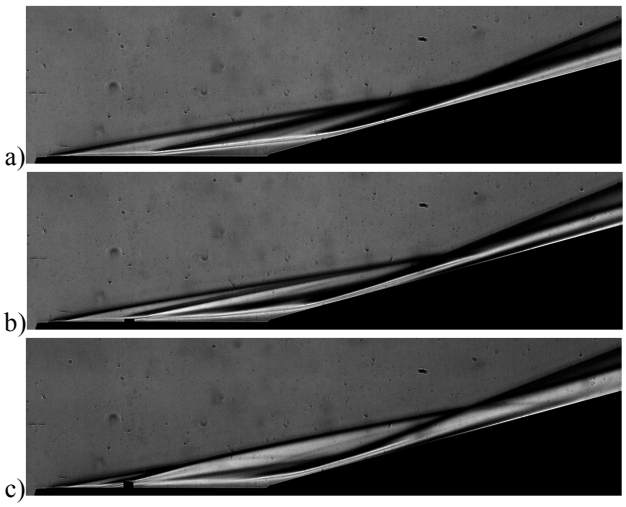

Fig. 5. Same as Fig. 4, Re group #3.

Similar effect was observed previously in both numerical and experimental investigations of compression corner flow behind blunt leading edge generating the entropy layer (see e.g. [1] for details and additional references). The roughness makes the reattached boundary layer thicker and smoothen the Schlieren images, which could point to earlier turbulization of the flow. The

tallest roughness of height k=1.2 mm (Fig. 4c) protrudes to the edge of the hypersonic boundary layer, which is close to the case of Re group #3 at k=0.6 mm (Fig. 5b). This leads to reduction of the separation bubble size at both Reynolds numbers. Thus, the separation zone elongates for small roughness heights and shrinks for large ones. The observed reversal trend seems to be relevant to the entropy layer effect.

Visible is a small separation region in front of the roughness rake (Fig. 4c, 5b, 5c). The roughness-induced shock wave interacts with the bow shock wave and pushes it aside of the surface. The flow is highly disturbed in the presence of the tallest roughness rake. The flow features becomes highly smoothened behind the reattachment.

At the highest Reynolds number and tall roughness rake, the separation bubble appears to shrink. This is supposed to be due to two main factors: earlier turbulization of reattached boundary layer or effect of intense streamwise vortices that are able to entrain high-momentum fluid into the mixing layer, thereby shortening the separation bubble.

One may note that the roughness rake placed at 17 mm downstream the leading edge does not pin the separation station to itself. Additional experiments with the roughness at 23.5 mm showed that separation became sensitive to the roughness height, especially for higher Reynolds number cases, when the separation occurred exactly at roughness station.

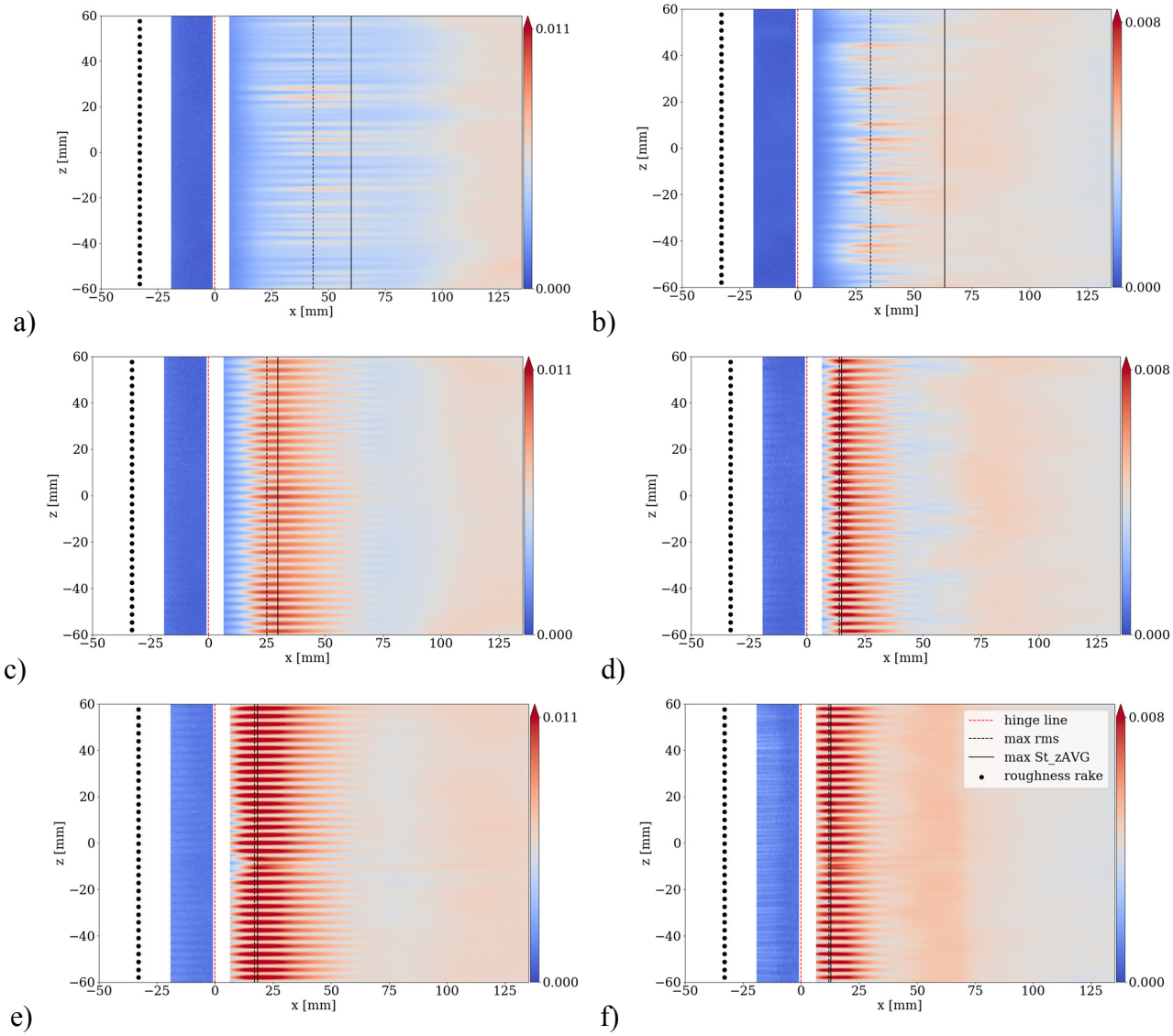

Fig. 6. Example distributions of St over the model surface k=0 (a,b), 0.6 (c,d) and 1.2 mm (e,f); Re group #1 (a,c,e) and #3 (b,d,f); view from the top. Leading edge is at x_{LE} = –50mm.

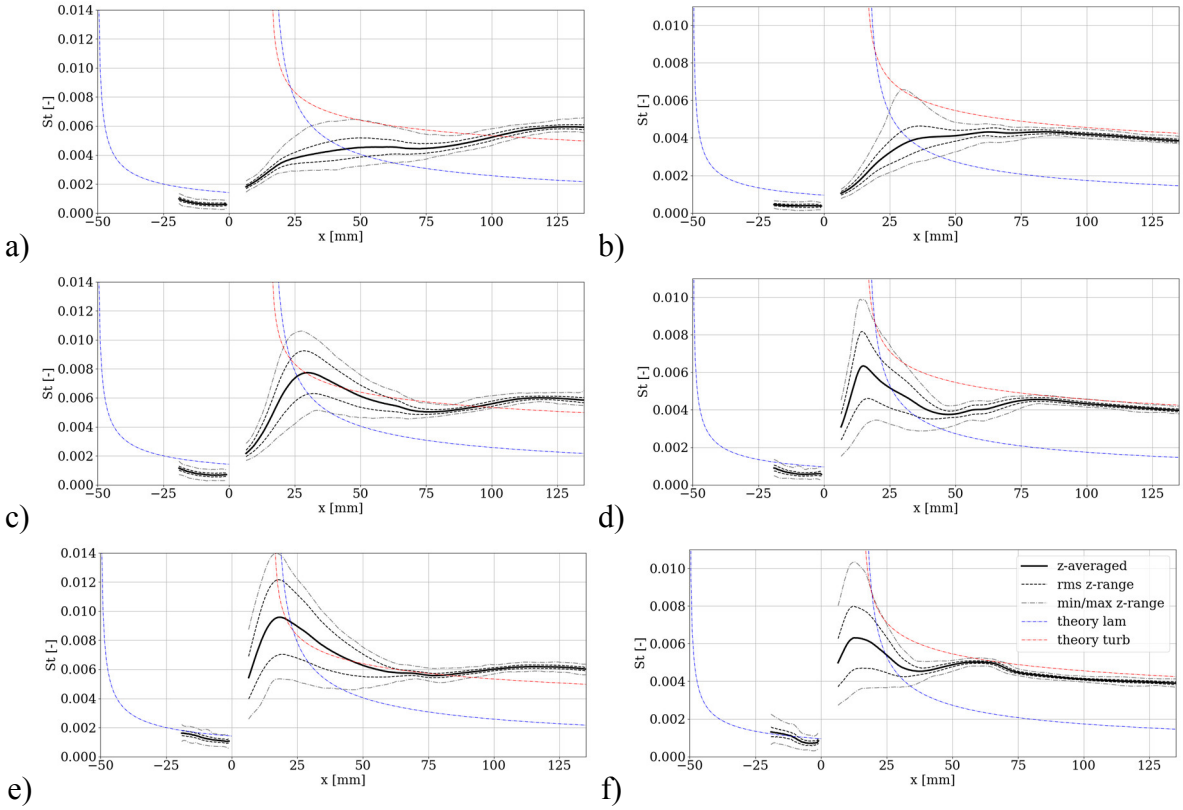

Fig. 7. Spanwise-averaged $St_{zAvg}(x)$ distribution with rms and min/max spanwise deviations due to vortices. Subfigures (a) and (b) correspond to Fig. 6; Eq. (4) defines the theory curves (see next section).

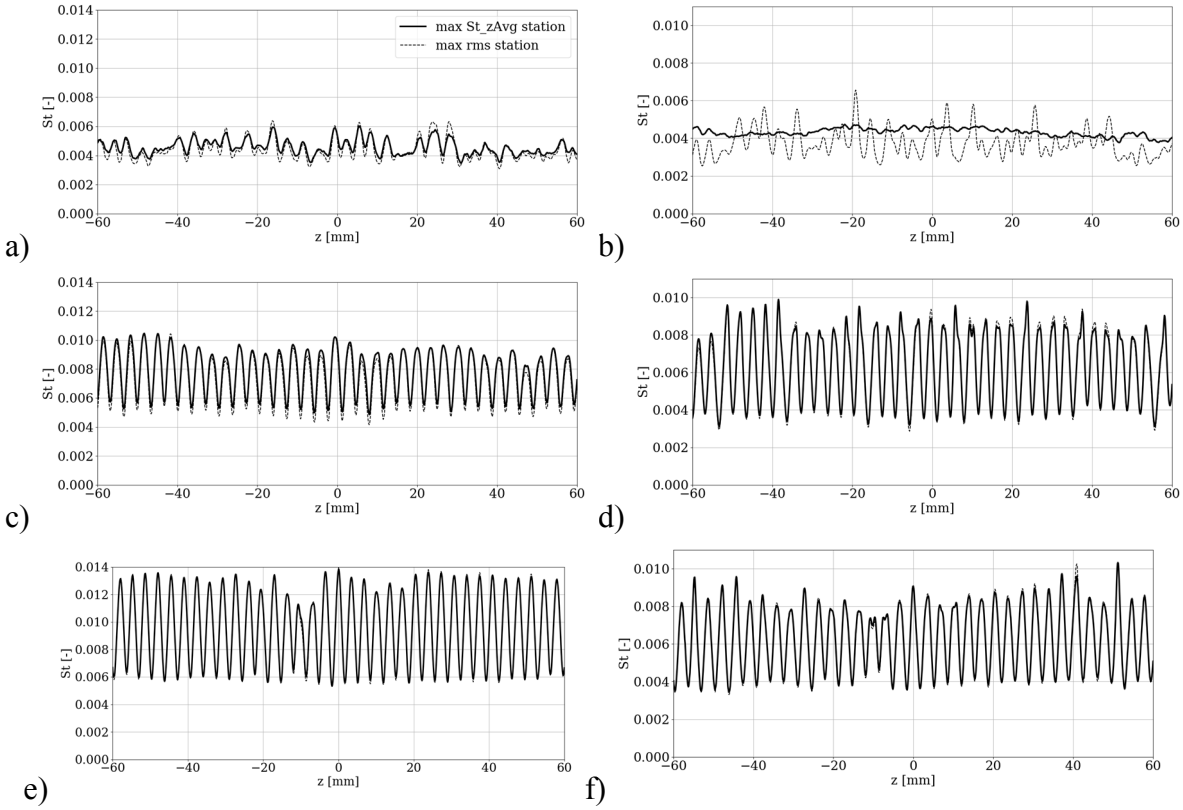

Fig. 8. Spanwise distribution $St(x_{max},z)$; x_{max} corresponds to the maximum station of either $St_{zAvg}(x)$ or its *rms* deviations. Subfigures correspond to Fig. 6

3.2 Thermal patterns

Figure 6 summarizes distribution of St over the model surface at roughness heights 0.0, 0.6, 1.2 mm (from top to bottom); left and right columns correspond to Re groups #1 and #3, respectively. The coordinates are plotted with respect to the hinge line that is 50 mm downstream from the leading edge. Dashed and solid lines represent the stations of maximum spanwise standard (rms) variations of St and maximum spanwize-averaged (z-averaged) value of St. The roughness station is marked with black circles (not in scale).

All experiments are done at low Reynolds numbers, which suggests near-laminar reattachment flow in accord to the criterion [6]. However, transition may not be excluded even for the smooth surface as discussed above. Figure 6 partially confirms the near-laminar reattachment at both Reynolds numbers: heat flux increases behind the region where vortices are observed most distinctly. These increases seem to correspond to ending laminar-turbulent transition process. Note the above discussion on Fig. 4a, where the weak bow shock wave reaches the surface at $x\approx71$ mm, which may trigger or somehow affect the transition process.

Despite the absence of the roughness rake (Fig. 6a,b), the reattachment flow is subjected to Görtler-type vortices that occur without being artificially excited. The spanwise variation of St due to vortices attain maximum on the dashed line behind both the reattachment and the neck. This station does not coincide with the local maximum of spanwise-averaged St distribution (black solid line). The two lines become closer as the roughness height increases, and they appear to coincide when roughness is rather tall.

Figures 7a, 7b illustrates z-averaged $St_{zAvg}(x)$ distribution that slowly rises downstream from the reattachment station. This should be attributed to the combined effect of vortices and possible transition, because the latter cannot be excluded based on the available data. This is more evident for Re group #3 where (possibly) turbulent level is attained faster. Note that St_{zAvg} for Re group #1 (Fig. 7a) attains maximum near $x_{max}\approx60$ mm and then begins decreasing, which is accompanied by noticeable attenuation of thermal footprint of vortices (Fig. 5a). Nevertheless, St_{zAvg} begins increasing again at $x\approx75$ mm, which points to the fact that regular streamwise vortices added more to heat flux in comparison with transition process for $x<75$ mm. This description should remain valid in purely laminar flow behind the reattachment. Thus, the vortices themselves may be able to increase the average heat transfer even if the flow is laminar.

The vortices being able to enhance the averaged heat transfer becomes more evident in the presence of the roughness rake, when the vortices are stronger than those induced naturally (see Fig. 6c–f and 7c–f). The maximum of St_{zAvg} is now very close to the neck station and well above the value for no roughness case. Again, the vortices quickly disappear downstream with more rapid reduction of St_{zAvg} until behavior of $St_{zAvg}(x)$ becomes similar to that for no roughness case (cf. Fig. 7a and 7b). In particular, this gives rise to very close (possibly turbulent) St levels by the end of the plate. Note the slight hump at $x\approx60$ mm for Re group #1 that presumably correspond to the fall of the weak bow shock.

The spanwise structure of vortices is illustrated in Fig. 6 and 8. It is rather chaotic for low heights of the roughness rake (Fig. 6a,b and 8a,b; k=0.0 mm) and changes when the sharp leading edge is polished or replaced (not shown here). The structure becomes regular following the location of the roughness elements. This, in particular, happens only for $k > 0.4$ mm in the case of Re group #1 (see e.g. Fig. 6c and 8c, k=0.6 mm).

It is also to be noted that a thermally visible part of the flat plate on the left hand of the hinge line (the red dashed line of Fig. 6) is inside the separation bubble for low roughness heights. The vortices are not visible there in thermal patterns, but the poor imprint of the roughness rake disturbances is present, which is clearly seen in Fig. 6e, 6f for the tallest roughness case.

3.3 Data reduction

Laminar boundary layer thickness over a sharp flat plate is evaluated as Ginoux [8]:

$$\frac{\delta}{x}\sqrt{\frac{\mathrm{Re}_{e,x}}{C^*}} = K + 2.21\frac{\gamma-1}{2}M_e^2 + 1.93\frac{T_w - T_{ad}}{T_e} \quad ,(2)$$

$$C^* = \frac{\mu^* T_e}{\mu_e T^*}$$

where K=5 for boundary layer thickness at u=0.99U_e, while K=1.72 for the displacement thickness, and C^* is a Chapman–Rubesin constant based on Eckert's reference temperature $T^* = 0.28T_e + 0.50T_w + 0.22T_r$. Recovery temperature is defined as $T_r = T_e \times (1 + 0.5r\,(\gamma\text{-}1) \times \mathrm{M_e}^2)$, with r=$\mathrm{Pr}^{0.5}$ for laminar boundary layer. Dynamic coefficient of viscosity is computed in accord with Sutherland's law:

$$\frac{\mu(T)}{\mu_{ref}} = \frac{T_{suth} + T_{ref}}{T_{suth} + T}\left(\frac{T}{T_{ref}}\right)^{1.5}, \qquad (3)$$

where T_{ref}=273.11 K, μ_{ref}=1.716×10^{-5} kg/(m·s), T_{suth}=*110.4* K.

Figure 8 shows the self-similar profiles $u(\eta)$, $T(\eta)$ that have been obtained numerically by solving compressible boundary layer equations for M_∞=8, T_0=*735 K*, T_w=*293 K*, Pr=0.72. Physical coordinates are recovered from the inner coordinate as $y=\eta x(\mathrm{Re}_{e,x})^{-0.5}$. For x_k=17 mm, the viscous interaction parameter $\chi=\mathrm{M}^3(\mathrm{C}/\mathrm{Re}_{\infty,xk})^{0.5}$ is 1.6 and 1.1 for Re group #1 and #3, respectively, which is not small to readily neglect the viscous-invscid interaction at the roughness station. Nevertheless, weak viscous-inviscid interaction is a good approximation to use for the reduction of the present experiments.

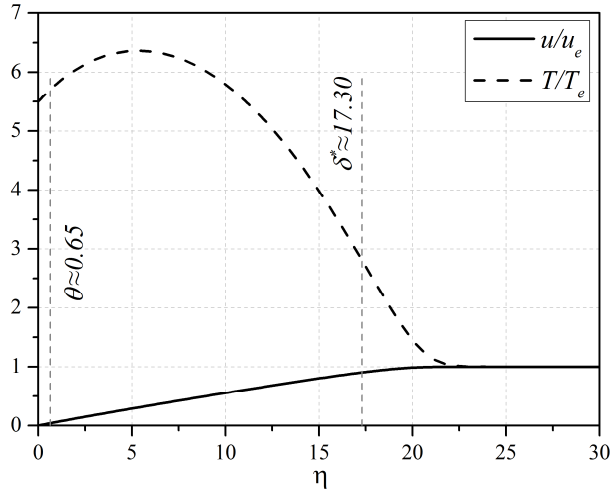

Fig. 8. Self-similar boundary layer profiles

The theoretical heat flux for zero-gradient flat plate flow is calculated as in [9]:

$$\mathrm{St}_{theory} = \frac{A}{s}\left(\frac{u_e p_e}{u_\infty p_\infty}\right)^{1-n}\left(\frac{T_\infty}{T^*}\right)^{1-2n}\left(\frac{C^*}{\mathrm{Re}_{\infty,x}}\right)^{n}, \qquad (4)$$

where constants A,s,n and r are 0.332, $\mathrm{Pr}^{2/3}$, 0.5, $\mathrm{Pr}^{1/2}$ and 0.0296, 1, 0.2, $\mathrm{Pr}^{1/3}$ for laminar and turbulent flows, respectively. The reference temperature T^* is computed here in accord with [10] which is a more accurate modification of the classical definition given above:

$$\frac{T^*}{T_e} = \begin{cases} 0.45 + 0.55\,T_w/T_e + 0.16r\dfrac{\gamma-1}{2}M_e^2, \text{lam;} \\ 0.5\left(1 + T_w/T_e\right) + 0.16r\dfrac{\gamma-1}{2}M_e^2, \text{turb.} \end{cases} \quad ,(5)$$

The local values u_e, p_e, T_e at the edge of the boundary layer over the wedge are determined using a two-tier inviscid relation above the separation bubble, i.e. including flow deflection on the separation shock (inclined at approx. 12.5° to the plate in accord with Schlieren images for laminar separation, see Fig. 4a, 5a), and the subsequent deflection to along the wedge surface. The virtual origin of two theoretical curves on the wedge (see Fig. 6) is the reattachment point obtained from the Schlieren images for the case k=0.0 mm (Fig. 6a, x_{rea}≈16 mm). The third theoretical curve is for laminar flat plate at free-stream parameters on the edge of the boundary layer.

To reduce experimental distributions of $\mathrm{St}(x,z)$, $x_{\max}$ station is found at which $\mathrm{St}_{zAvg}(x)$ attains its local maximum near the reattachment. Next, $\mathrm{St}(x_{\max},z)$ is analyzed to find its min/max and standard deviation from the mean level:

$$rms \equiv rms\left(x_{\max}\right) = \\ = \sqrt{\frac{1}{N_i}\sum_{i=1}^{N_i}\left[\mathrm{St}\left(x_{\max}, z_k\right) - St_{zAvg}\left(x_{\max}\right)\right]}, \qquad (6)$$

where N_i is the number of pixels in spanwise direction of TSP image. The distribution of $\mathrm{St}_{\max}$ = $\mathrm{St}_{zAvg}(x_{\max})$ versus k/δ_k is then subjected to nonlinear fitting with logistic curve:

$$f(x) = A_1 + \frac{A_2 - A_1}{1 + \left(x/x_0\right)^a}. \qquad (7)$$

Polynomial fitting of 4th order is also used.

To process experimental data an interactive software has been developed using Python programming language and scientific libraries Qt5, numpy, scipy, etc.

3.4 Heating at reattachment

Consider distributions of $St_{zAvg}(k/\delta_k)$ plotted in Fig. 9. All experiments have been performed for close Reynolds numbers (groups #1 and #3) and the roughness station remains unchanged. Thus, the value of boundary layer thickness changes marginally from run to run within a Re group: δ_k = 1.42±0.02 mm (#1) and 0.95±0.02 (#3), and k/δ_k varies nearly linearly with k within each Re group.

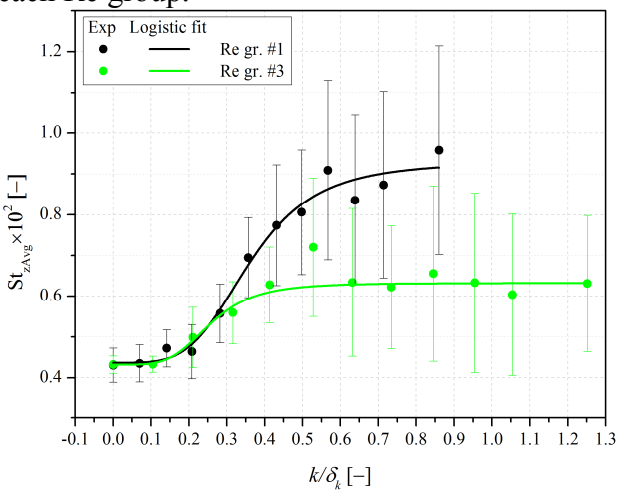

Fig. 9. Distribution of maximum z-averaged value of St with corresponding rms (error bars, see Eq.(6)).

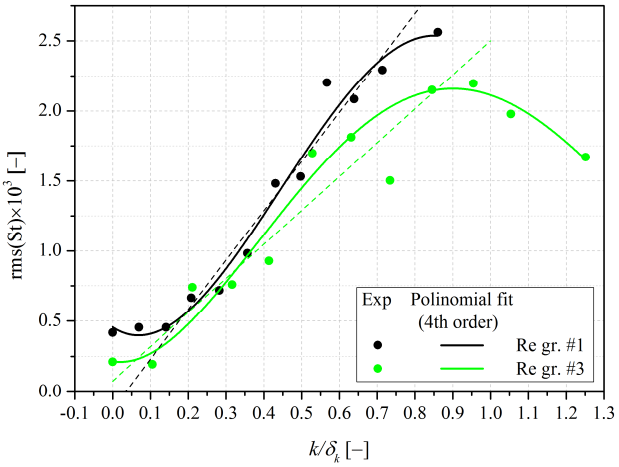

Fig. 10. Dependence of rms (see Eq.(6)) on roughness height

Consider the case of Re group #1. At low roughness heights, $k/\delta_k < 0.2$, the St_{max} does not appears to respond to the presence of roughness rake. Surface distributions of St remain close in amplitude with no roughness case (see Fig. 6a). At some critical value $(k/\delta_k)_{cr} \approx 0.2$ the value of St_{max} starts increasing. $St(x,z)$ field at reattachment begins bearing the imprint of the roughness rake at the next closest point $k/\delta_k \approx 0.28$. Accounting for the presence of natural streamwise vortices, this behavior could mean that natural disturbances are stronger than those seeded by the roughness rake of $k/\delta_k < (k/\delta_k)_{cr} \approx 0.2$.

The results suggest that the rising trend saturates for large roughness elements, which might correspond to the fact that the roughness elements are located rather close to each other and begin working like a solid 2D spanwise roughness trip-strip when the height k becomes large. The spacing-to-diameter ratio of roughness elements is two, which makes this suggestion possible [5].

Despite the saturation of St_{zAvg}, the spanwise deviation of St at station x_{max}, *rms* of Eq. (6), does not saturate (see Fig. 10) as k/δ_k rises. It is close to constant for $k/\delta_k<(k/\delta_k)_{cr}$ and start increasing nearly linearly for approx. $k/\delta_k>(k/\delta_k)_{cr}$. One should note that Re group #3 curve has reduced values of *rms* at $k/\delta_k<0.2$ because the station x_{max} is in the region where the vortices are nearly contaminated (see Fig. 6b and 8b). The corresponding values at the station of maximum standard spanwise deviations of St are close to those of the Re group #1, making the values of $(k/\delta_k)_{cr}$ similar for both Re groups considered. Extension of the regression lines over the nearly linearly rising portion of data to lower values of k/δ_k comes close to zero. The two statements are following. First, spanwise standard variation of St due to vortices is linearly dependent on the height of the seeding roughness rake unless the height exceeds some threshold value ($k/\delta_k \approx 0.8$), with no variation at no roughness (linear receptivity of boundary layer to the height of the roughness rake). Second, natural level of disturbances that turn into Görtler vortices at reattachment correspond to the roughness of the critical height.

4 Conclusion

Experimental investigation of the effect of Görtler-like vortices on heat transfer in nominally two-dimensional compression corner flow has been carried out at Mach 8, Reynolds numbers based on the flat plate length $(1.77\pm0.08)\times10^5$ and $(3.90\pm0.15)\times10^5$, and wall-

to-stagnation temperature ratio 0.40. The experiments include Schlieren imaging and TSP measurements. The vortices have been induced naturally (by themselves) or artificially by using a rake of cylindrical roughness elements of heights from 0.1 to 1.2 mm, 1.7 mm diameter and 3.4 mm spacing. The state of boundary layer at reattachment is laminar or transitional.

The vortices are capable of increasing the spanwise-averaged heat flux behind the reattachment region independent on the state of the boundary layer. This effect may confuse the comparison of numerical and experimental results. The effect saturates as the roughness height reaches the value of the boundary layer thickness. Spanwise standard variation of heat transfer coefficient increases nearly linearly with roughness height, with no variation at no roughness (nearly linear receptivity). This proceeds unless the roughness height-to-boundary layer thickness ratio reaches a particular value of approx. 0.8 and the rising behavior turns to decreasing one.

Acknowledgements

The work has been carried out in Central Aerohydrodynamic Institute under the support of Russian foundation for basic research (project no. 17-08-00567). Compressible boundary layer solver has been developed in Moscow Institute of Physics and Technology under the support of Russian scientific foundation (project no. 14-19-00821) and adapted for the purpose of the present study.

References

[1] Chuvakhov P.V., Borovoy V.Ya., Egorov I.V., Radchenko V.N., Olivier H, and Roghelia A. Effect of Small Bluntness on Formation of Görtler Vortices in a Supersonic Compression Corner Flow. *Journal of Applied Mechanics and Technical Physics*, Vol. 58, No. 6, pp. 975–989, 2017.

[2] Simeonides G. and Haase W. Experimental and Computational Investigations of Hypersonic Flow about Compression Ramps. *J. Fluid Mech.*, Vol. 283, No. 1, pp. 17–42, 1995.

[3] Chuvakhov P.V., Egorov I.V., Olivier H., and Roghelia A. Joint Influence of High Entropy Layer and Goertler Vortices on Heat Transfer in Supersonic Compression Ramp Flow. *Computational Thermal Sciences: An International Journal*, Vol. 8, No. 6, pp. 543–553, 2016.

[4] Sivasubramanian J. and Fasel H.F. Direct Numerical Simulation of Transition in a sharp cone boundary layer at Mach 6: fundamental breakdown. *J. Fluid Mech.*, Vol. 768, pp. 175–218, 2015.

[5] Schneider S.P. Effects of Roughness on Hypersonic Boundary-Layer Transition. *Journal of Spacecraft and Rockets*, Vol. 45, No. 2, pp. 193–209, 2008.

[6] Hung F. and Barnett D. Shockwave-boundary layer interference heating analysis. *11th Aerospace Sciences Meeting*, AIAA Paper No. 73–237, 1973.

[7] Mosharov V.E. and Radchenko V.N. Measurements of heat flux fields in short-duration wind tunnels by temperature-sensitive paints. *Uch. Zap. TsAGI*, Vol. 38, No. 1-2, pp. 94–101, 2007, in Russian.

[8] Ginoux J.J. *Laminar Boundary Layers.* Course note 104, von Karman Institute for Fluid Dynamics, Rhode-Saint-Genèse, 1978.

[9] Simeonides G. Hypersonic shock wave boundary layer interactions over compression corners. *Ph.D. Thesis*, University of Bristol, 1992.

[10] Meador W.E. and Smart M.K. Reference enthalpy method developed from solutions of the boundary-layer equations. *AIAA J.*, Vol. 43, pp. 135–139, 2005.

Contact Author Email Address

mailto:pavel_chuvahov@mail.ru

Copyright Statement